ADVANCED ELECTRONIC MATERIALS
www.advelectronicmat.de

Artificial Astrocyte Memristor with Recoverable Linearity for Neuromorphic Computing

Caidie Cheng, Yanghao Wang, Liying Xu, Keqin Liu, Bingjie Dang, Yingming Lu, Xiaoqin Yan, Ru Huang,* and Yuchao Yang**

Neuromorphic systems provide a potential solution for overcoming von Neumann bottleneck and realizing computing with low energy consumption and latency. However, the neuromorphic devices utilized to construct the neuromorphic systems always focus on artificial synapses and neurons, and neglected the important role of astrocyte cells. Here, an astrocyte memristor is demonstrated with encapsulated yttria-stabilized zirconia (YSZ) to emulate the function of astrocyte cells in biology. Due to the high oxygen vacancy concentration and resultant high ionic conductivity of YSZ, significantly lower forming and set voltages are achieved in the artificial astrocyte, along with high endurance (>10^{11}). More importantly, the nonlinearity in current-voltage characteristics that usually emerge as the testing cycle increases can be depressed in the astrocyte memristor, and the nonlinearity can also be reversed by applying a refresh operation, which implements the role of biological astrocyte in maintaining the normal activity of neurons. The recovery of linearity can dramatically improve the accuracy of Modified National Institute of Standards and Technology dataset classification from 62.98% to 94.75% when the inputs are encoded in voltage amplitudes. The astrocyte memristor in this work with improved performance and linearity recovery characteristics can well emulate the function of astrocyte cells in biology and have great potential for neuromorphic computing.

1. Introduction

Traditional von Neumann architecture has encountered a fundamental bottleneck due to the separation of storage and computing modules.[1–3] Neuromorphic computing, which simulates the computing architecture and functionalities of the human brain, has received widespread attention for solving this problem.[4–8] Therefore, neuromorphic devices, which are the most basic unit of neuromorphic computing, have also become a hot topic for research.[9–15] In particular, memristors with simple structure and high performance can be utilized as the most potential candidates for the hardware implementation of neuromorphic computing.[11,16,17] There are many current researches on memristive devices to study the function of synapses[18–20] and neurons[21–23] as they are the foundation of the brain to realize memory and learning functions.[24,25] However, in biology, as the surrounding environment of the synapse, astrocytes also have an important influence on the synaptic signal transmission and thus affect the expression of information.[26,27] In fact, the neurotransmitters released by the pre-synaptic membrane are not only received by the post-synaptic, but also by astrocytes. The absorption activities of the neurotransmitters accompanied by the outflow activity of potassium ions can activate astrocyte cells to release gliotransmitters, such as glutamate, adenosine triphosphate, D-serine, homocysteine, etc. which will affect the signal transmission of synapses between neurons.[28]

Herein, an artificial astrocyte memristor with encapsulated layer is fabricated to emulate the function of astrocyte on synapse in biology. Due to the doping of Y^{3+} with lower valence into ZrO_2, the yttria-stabilized zirconia (YSZ) material with high oxygen vacancy concentration and resultant high ionic conductivity can be obtained to maintain charge neutrality and in turn serves as the encapsulated layer,[29–33] while TaO_x has relatively lower dielectric constant than YSZ adopted as switching layer.[34,35] The resultant astrocyte memristor with a structure of YSZ:(Pt/Ti/TaO_x/Au) exhibits high endurance (>10^{11}). Compared with devices without encapsulated layer, the forming and set voltages are reduced significantly, due to oxygen vacancies supplied from YSZ. More importantly, as the cycling number increases, the nonlinearity of current-voltage

C. Cheng, X. Yan
State Key Laboratory for Advanced Metals and Materials
School of Materials Science and Engineering
University of Science and Technology Beijing
Beijing 100083, China
E-mail: xqyan@mater.ustb.edu.cn
C. Cheng, Y. Wang, L. Xu, K. Liu, B. Dang, Y. Lu, R. Huang, Y. Yang
Key Laboratory of Microelectronic
Devices and Circuits (MOE)
School of Integrated Circuits
Peking University
Beijing 100871, China
E-mail: ruhuang@pku.edu.cn; yuchaoyang@pku.edu.cn
R. Huang, Y. Yang
Center for Brain Inspired Chips
Institute for Artificial Intelligence
Peking University
Beijing 100871, China
R. Huang, Y. Yang
Center for Brain Inspired Intelligence
Chinese Institute for Brain Research (CIBR)
Beijing 102206, China
The ORCID identification number(s) for the author(s) of this article can be found under https://doi.org/10.1002/aelm.202100669.

DOI: 10.1002/aelm.202100669

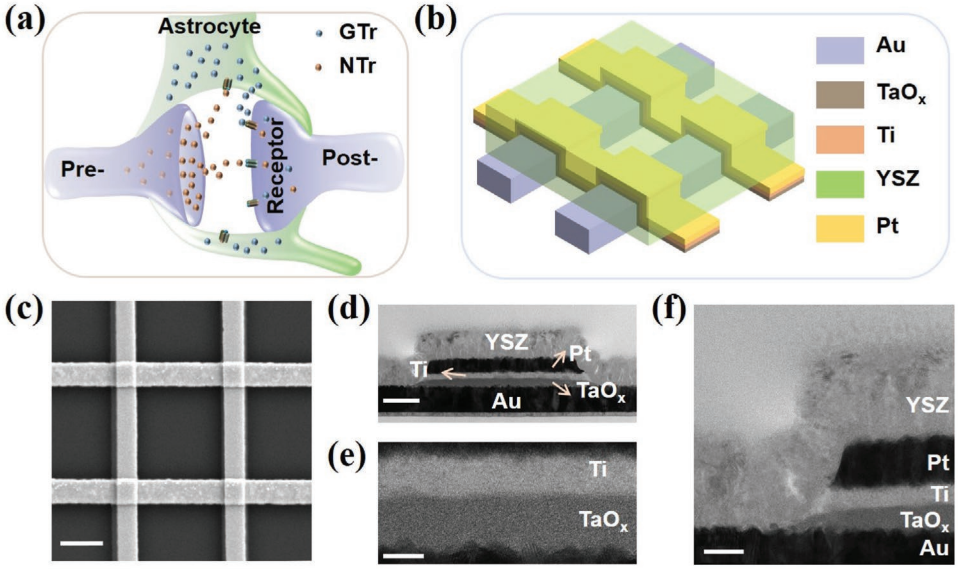

Figure 1. a) Schematic of the Astrocyte in biological systems. The GTr is the abbreviation for gliotransmitter, as the NTr is the abbreviation for neurotransmitter. b) The schematic of the astrocyte memristor with an encapsulated structure in this work. c) SEM micrograph of 2 × 2 astrocyte memristor array with a device size of 250 nm. Scale bar: 500 nm. d) TEM image of the Astrocyte's cross-section structure which is analogous to the astrocyte cell in biology. Scale bar: 50 nm. e) HRTEM image of the Astrocyte in the center region. Scale bar: 10 nm. f) HRTEM image of the Astrocyte in the sidewall region. Scale bar: 20 nm.

(*I-V*) characteristics becomes evident, however, the astrocyte memristor shows remarkable recovery ability of linearity with simple refresh operations. By combining this recoverable linearity with a multi-layer perceptron network for inference where the voltage amplitude is used to encode input images, the accuracy in the recognition of Modified National Institute of Standards and Technology dataset (MNIST) images can be improved from 62.98% to 94.75%. The achievement of astrocyte memristor with enhanced performance and recoverable linearity has great potential in neuromorphic computing.

2. Results and Discussion

The schematic diagram of synapse encapsulated by astrocytes in biological systems is illustrated in **Figure 1**a, where the astrocyte closely interacts with the activity of synapse. Inspired by this, a memristor-based artificial astrocyte with an encapsulated structure is proposed to implement the function of the astrocyte (Figure 1b). Figure 1c shows the scanning electron microscopy (SEM) image of a 2 × 2 astrocyte memristor array with a device size of 250 nm. In particular, Pt/Ti/TaO_x/Au memristor is utilized to realize traditional artificial synapse, while the YSZ coated on the sidewall of the Pt/Ti/TaO_x/Au device is analogous to the astrocyte cell in biology, as displayed in Figure 1d. High-resolution transmission electron microscope (HRTEM) images of the astrocyte memristor in the center and sidewall regions are shown in Figure 1e,1f, clearly showing the encapsulated sidewall of the devices. The YSZ:(Pt/Ti/TaO_x/Au) device is therefore structurally analogous to biological astrocytes.

We first studied the characteristics of traditional Pt/Ti/TaO_x/Au memristive devices without the YSZ astrocyte layer, which is named N-astrocyte synapse, as displayed in **Figure 2**. A forming process of ≈6 V is required to activate the N-astrocyte memristors (inset of Figure 2a). Figure 2a shows the *I-V* curves in 100 consecutive cycles of the N-astrocyte memristors, where the nonlinearity of the low resistance state (LRS) gradually increases as the number of sweeping increases. It is worth noting that here the nonlinearity refers to is that in the dependence of current on voltage, instead of the nonlinearity in conductance modulation of artificial synapses with respect to identical pulses. Figure 2b shows the pulse measurement results, where the alternate positive pulse of (+2.5 V, 50 ns) and negative pulse of (–2.7 V, 50 ns) are applied, showing reliable resistive switching. Figure 2c further shows that the endurance of the Pt/Ti/TaO_x/Au synapse is more than 10^5 with an on /off ratio of ≈15 under pulse conditions. The nonlinearity in the on state of *I-V* characteristics are monitored during the endurance measurements by a set of consecutive DC sweeps after (10^1, 10^2, 10^3, 10^4, and 10^5) cycles, and the corresponding *I-V* characteristics are shown in Figure S1, Supporting Information, and the inset of Figure 2d. One can see an obvious decrease in on/off ratio (Figure 2c) and an increase of nonlinearity (Figure S1, Supporting Information) as the cycling number increases. Such nonlinearity in on state is quantitatively measured and summarized in Figure 2d, showing clearly that the nonlinearity of on state increases as a function of the cycling number. This might be attributed to the depletion of oxygen vacancies in TaO_x, which are involved in the formation and rupture of filaments but are driven toward the electrodes during repetitive switching process. There are in general two ways to define the *I-V* nonlinearity of LRS. One is to define nonlinearity as $I_V/I_{V/2}$, where V is the reading voltage of a fixed value.[36,37] Instead, the relationship between current and voltage can be fitted as $I = a*V + b*V^{(2+c)}$ where the coefficient (2+c) determines the degree of nonlinearity.[38] For the sake of universality, we utilized the

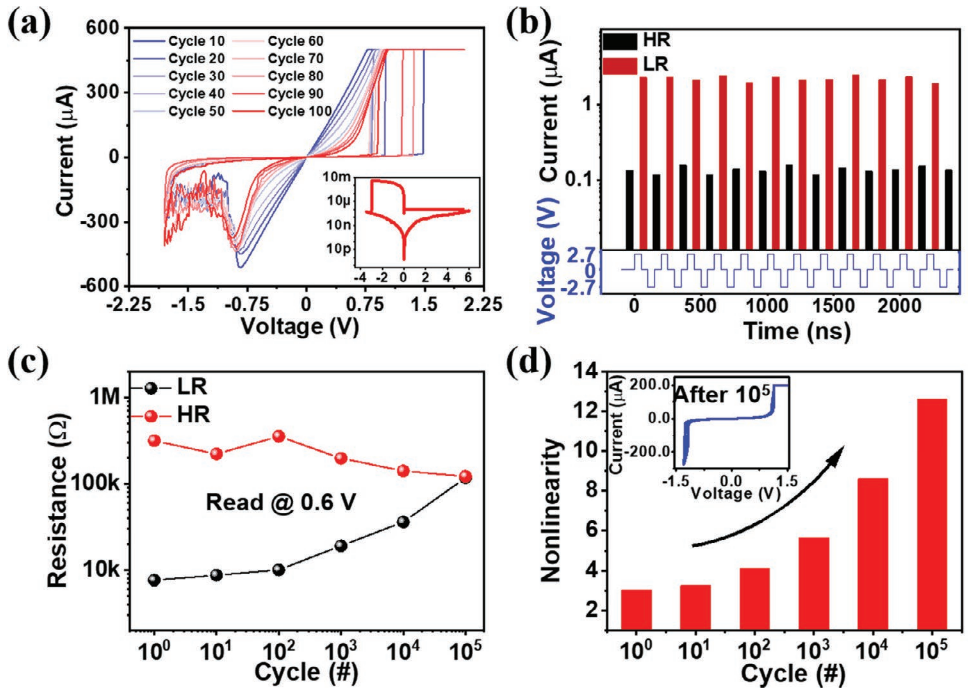

Figure 2. Electrical characterization of N-astrocyte memristor. a) *I-V* curves of the N-astrocyte memristor under the different cycle tests. The inset shows the forming process with the voltage of ≈6 V. b) Current responds under the alternate single positive pulse of (+2.5 V, 50 ns) and negative pulse of (−2.7 V, 50 ns). The reading voltage for measuring the resistance of the devices is 0.1 V. c) Endurance test of the N-astrocyte memristor. The reading voltage for measuring the resistance of the devices is 0.6 V. d) Nonlinearity factor distribution as a function of the endurance tests. The inset shows the *I-V* characteristic after 105 endurance tests.

second approach to quantitatively extract the *I-V* nonlinearity of devices.

Besides traditional two-terminal Pt/Ti/TaO_x/Au memristive synapse, we have further studied the artificial astrocyte, where 40 nm YSZ encapsulation layer was deposited around the Pt/Ti/TaO_x/Au cell so that the TaO_x switching layer is in direct contact with the surrounding YSZ medium, that is, YSZ:(Pt/Ti/TaO_x/Au). **Figure 3**a shows *I–V* characteristics of the astrocyte memristors in 100 consecutive cycles. Notably, the forming voltage of the device was reduced to ≈3 V, in contrast to the ≈6 V forming voltage of Pt/Ti/TaO_x/Au device with the same TaO_x thickness (Figure S2, Supporting Information). One can also see from the consecutive *I–V* measurements that excellent uniformity is realized in the YSZ:(Pt/Ti/TaO_x/Au) artificial astrocyte, and the LRS remains approximately linear throughout the sweeping cycles, in stark contrast to Pt/Ti/TaO_x/Au device where significant *I–V* nonlinearity has emerged in 100 cycles (Figure 2a). Figure 3b,3c further exhibits gradual potentiation and depression of the device by incrementally altering the current compliance of the set process and the sweeping voltage of the reset process, respectively. Figure 3d further shows the pulse measurement results of YSZ:(Pt/Ti/TaO_x/Au) artificial astrocyte, where the alternate positive pulse of (+1.6 V, 50 ns) and negative pulse of (−1.8 V, 50 ns) are applied, showing reliable resistive switching. The endurance of the device is significantly improved, which has reached 10^{11} with an on/off ratio of ≈40, as shown in Figure 3e. Both the improved *I–V* linearity and endurance can be attributed to the inclusion of YSZ astrocyte medium around the device, which can act as an oxygen vacancy reservoir and therefore compensate the depletion of oxygen vacancies during the repetitive switching process in both DC (Figure 3a) and pulse (Figure 3d) schemes. The YSZ:(Pt/Ti/TaO_x/Au) device, therefore, implements the role of biological astrocytes in maintaining the normal activity of neurons in the case of individual synaptic necrosis. Moreover, the astrocyte memristor demonstrates retention of >10^6 s without noticeable degradation.

The nonlinearity of the YSZ:(Pt/Ti/TaO_x/Au) artificial astrocyte memristor is also monitored during the endurance tests, as shown in **Figure 4**a. One can see that the increase of nonlinearity slows down dramatically, which remains almost unchanged in 10^7 cycles and is ≈5 after 10^{11} cycles, in stark contrast to the high nonlinearity of ≈12 after only 10^5 cycles in Pt/Ti/TaO_x/Au devices (Figure 2d). Intriguingly, the linearity of the YSZ:(Pt/Ti/TaO_x/Au) artificial astrocyte can be recovered by a refresh operation, by applying a pair of strong voltage pulses (±3.5 V, 50 ns). Figure 4b shows the *I–V* characteristics before and after the refresh operation, showing that the strongly nonlinear *I–V* after 10^{11} endurance test returns to a state with high linearity. Figure 4c further shows the nonlinearity factor distribution with and without the refresh operation in different endurance cycles, demonstrating that good linearity can be maintained throughout 10^{11} cycles. This can once again be attributed to the oxygen vacancy supplement from the YSZ medium, as schematically depicted in **Figure 5**, which compensates the depletion of oxygen vacancies during resistive switching similar to the role of biological astrocyte, therefore

ADVANCED ELECTRONIC MATERIALS
www.advelectronicmat.de

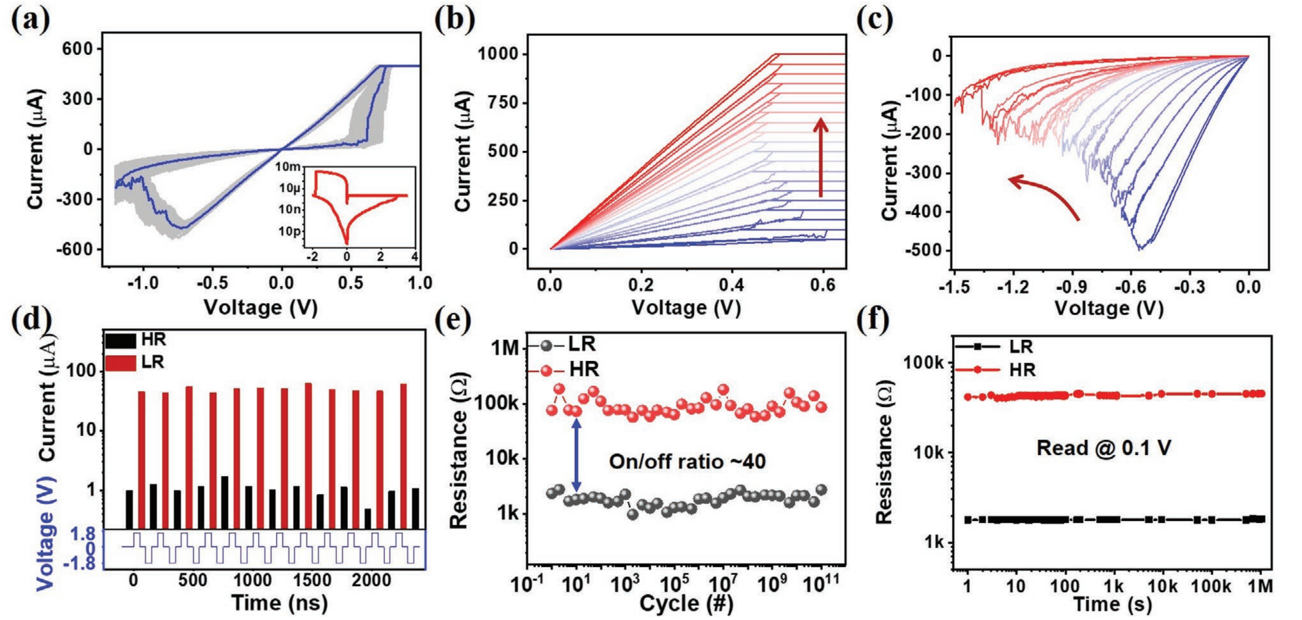

Figure 3. Electrical characterization of astrocyte memristor. a) 100 consecutive *I-V* curves of an astrocyte memristor. The inset shows the forming process with the voltage of ≈3 V. b) Gradual potentiation by incrementally altering the current compliance. c) Gradual depression under the negative voltage sweeping. d) Current responds under the alternate single positive pulse of (+1.6 V, 50 ns) and negative pulse of (−1.8 V, 50 ns). e) Endurance tests of the N-astrocyte memristor, indicating endurance of $>10^{11}$ cycles. f) Retention characteristic of N-Astrocyte with the read voltage of 0.1 V, showing high retention of $>10^6$ s.

maintaining a relatively stabilized oxygen vacancy profile in the memristor.

It should be noted that the reset voltages of the two kinds of memristors are higher than set voltages. Therefore, after excessive cycling processes, it results in the accumulation of oxygen vacancies near the top electrode interface,[39–41] as shown in Figure 5c, which leads to the appearance of nonlinearity. The depletion of oxygen vacancies in the TaO_x layer, however, can be compensated by the diffusion of oxygen vacancies into TaO_x from YSZ following the concentration gradient, leading to the recovery of linearity (Figure 5c). It should be noted that the lateral size of the astrocyte memristor was designed to be rather small, namely 250×250 nm^2, so as to enhance the role of the encapsulated layer, and the physical size of filaments can actually be tens to a hundred nanometers in oxide memristors[39,42] and previous studies have also supported the existence of multiple filaments.[43] The location(s) of the conductive filament(s) is determined by the defect distribution inside the switching material,[42,44,45] without necessarily sitting in the center of the device. Given these physical attributes of the filaments, we expect a significant impact of the YSZ encapsulated layer on the 250×250 nm^2 device, which allows oxygen vacancies from the YSZ to modulate the linearity of the astrocyte memristor following the concentration gradient. Application of strong voltage pulses can induce thermal effect and hence accelerate the diffusion and redistribution of oxygen vacancies in the switching and encapsulation layers, accounting for the quick recovery after the refresh operation (Figure 4b,c).

The nonlinearity in *I-V* characteristics can significantly affect the accuracy of vector-matrix multiplication and therefore

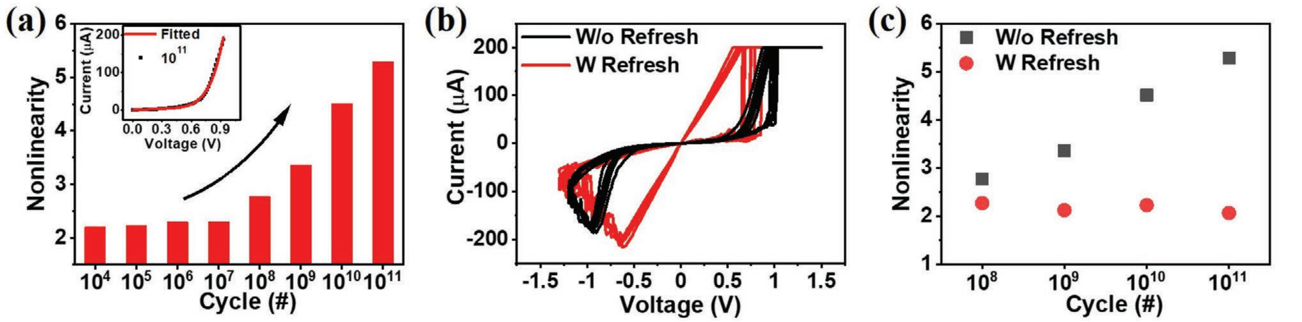

Figure 4. a) Nonlinearity factor distribution as the function of the endurance cycle in the astrocyte memristor. b) *I-V* characteristics with and without refresh (after the 10^{11} endurance test), by applying a pair of strong voltage pulse (±3.5 V, 50 ns). c) Nonlinearity factor distribution with and without refresh operation, indicating the recovery of the linearity under the operation of a refresh.

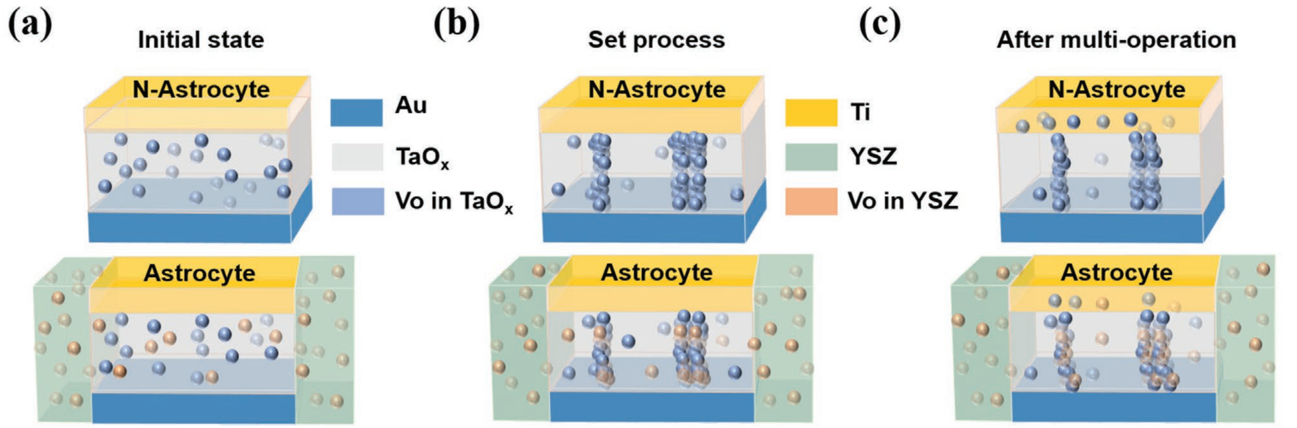

Figure 5. Schematic illustration of the physical switching mechanism of the nonlinearity recovery. a) The initial states of the N-Astrocyte and Astrocyte, respectively. b) The set processes of the N-Astrocyte and Astrocyte in the earliest stage. c) The set processes of the N-Astrocyte and Astrocyte after multi-operation, indicating the distribution of oxygen vacancies apparently extends into the Ti/TaO_x interface under the unequal set and reset stimulations.

the neural network performance when the input vectors are encoded in pulse amplitudes (**Figure 6**a).[38,46,47] To evaluate the effect of artificial astrocyte memristor in artificial neural networks, a multilayer perceptron network has been constructed with ternary weight precision and trained by a backpropagation algorithm (Figure 6a). This network has a fully connected structure and aims to classify ten handwritten digits from MNIST dataset, whose image size is 28×28. As shown in Figure 6a, the perceptron has 784 neurons for the input layer, 200 neurons for the hidden layer, as well as 10 neurons for the output layer. When a test image is fed into the network, the index of the neuron with maximum output implies the classification result. The input test image is encoded by the voltage amplitude, while the connection weights are extracted from the *I-V* characteristics in the experiment with the size of 784×200, and the bitmaps of the weight matrix between the input layer and hidden layer with different nonlinear data input are extracted. As the weight precision is ternary, the black pixel in the bitmaps represents the value −1, the white pixel is assigned the value of 1, and 0 is the gray pixel located between −1 and 1. Figure 6b shows the original 784×200 weight matrix of the first layer of connections with ideal linearity (upper), weight matrix of the first layer of connections as a result of nonlinearity after 10^8 endurance cycles (middle), and weight difference between the upper and

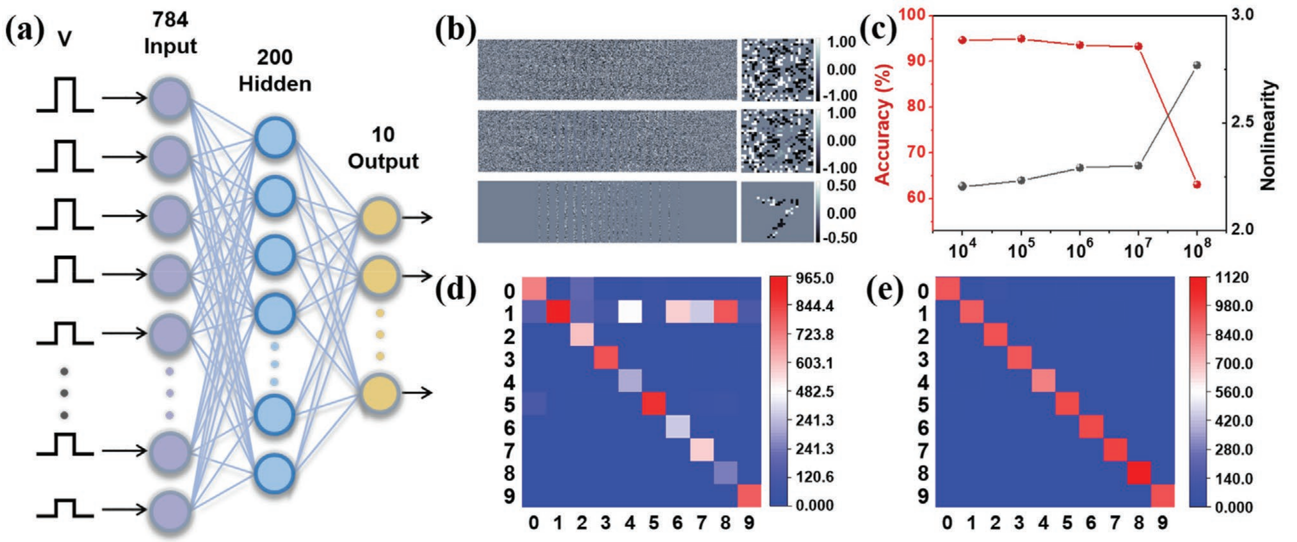

Figure 6. a) Illustration of testing processes of MNIST handwritten dataset using a double-layer perceptron network. b) Original 784×200 weight matrix of the first layer of connections with ideal linearity (upper), weight matrix of the first layer of connections as a result of nonlinearity after 10^8 endurance cycles (middle), and weight difference between the upper and middle panels (lower). A 28×28 weight matrix is extracted and reshaped from the first row of the respective matrices and shown on the right to show the difference clearly. c) The accuracy of MNIST image recognition as the function of endurance cycle in the astrocyte memristor, which decreases as the increase of nonlinearity. d) The recognition results of ten digits after 10^8 cycles without refresh with the accuracy of 62.98%. e) The recognition results of ten digits after 10^8 cycles with refresh, having the improved accuracy of 94.75%.

ADVANCED ELECTRONIC MATERIALS
www.advelectronicmat.de

middle panels (lower). A 28 × 28 weight matrix is extracted and reshaped from the first row of the respective matrices and shown on the right to show the difference clearly. It can be seen that the increase in nonlinearity results in significant changes in the weight matrix. The accuracy of the recognition as a function of the endurance cycle is demonstrated in Figure 6c, where a sharp drop of recognition accuracy after 10^8 endurance cycles is demonstrated, and the recognition results of ten digits are displayed in Figure 6d with an accuracy rate of 62.98%. This is due to the degradation of the linearity in the device, which significantly affects the information coding. Interestingly, after the linearity is recovered after refresh with big pulse stimulations, the recognition accuracy after the 10^8 cycles can be improved to 94.75%, as the recognition results of ten digits are demonstrated in Figure 6e. This unambiguously demonstrates that the astrocyte memristor has a great advantage in achieving stable, high-performance neural network accelerators, especially when the input information is encoded in pulse amplitudes.

3. Conclusion

In this study, we demonstrate an astrocyte memristor with encapsulated YSZ to emulate the function of astrocyte cells for synapse in biology. Due to the high oxygen vacancy concentration and resultant high ionic conductivity of the YSZ material, lower forming and set voltages were realized in the astrocyte memristor, along with high endurance ($>10^{11}$). Besides, the nonlinearity of current-voltage characteristics increases as the cycling number of devices increases. Interestingly, such nonlinearity can be reversed by applying high voltage stimulations, which is similar to the fact that astrocytes can maintain the normal activity of neurons in the case of individual synaptic necrosis. The recovery of linearity can dramatically improve the accuracy of MNIST image recognition from 62.98% to 94.75% under the 10^8 endurance measurements. The achievement of astrocyte memristor with improved performance and recovery characteristics of nonlinearity enrich the function of the memristors, indicating the great potential of memristor for neuromorphic computing.

4. Experimental Section

Device Fabrication: The astrocyte memristor device and N-astrocyte memristor were fabricated on the silicon substrate with 120 nm thermally grown SiO_2 with the same fabrication process. The electron beam lithography process was used to prepare the nano-scale devices. The bottom electrode with 5 nm/30 nm Ti/Au was deposited by electron beam evaporation following by a Lift-off process, and the metal Ti was served as an adhesion layer. Subsequently, the 15 nm Ta_2O_5 was deposited by radio-frequency magnetron sputtering at room temperature in Ar atmosphere. It is worth noting that the switching layer was patterned together with the top electrode. And then a lift-off process was performed following the deposition of 20 nm top electrode Ti and 10 nm protective layer Pt. The resultant devices have a size of 250×250 nm^2. At this point, the preparation of N-astrocyte memristor has been completed. In order to fabricate the astrocyte memristor, the last photolithography process was performed to prepare the encapsulated layer YSZ which was deposited by radio-frequency magnetron sputtering with the thickness of 40 nm followed by a lift-off process.

Electrical Measurements: Electrical measurements were performed to analyze the resistive switching characteristics using Agilent B1500A semiconductor parameter analyzer, while the oscilloscope sampling unit was connected to the B1500 to measure the single pulse response of the device. During all the measurements, the voltages were applied to the top electrode and the bottom electrode was always grounded.

Microstructural Characterization: The high-resolution scanning electron microscopy (HR-SEM) images were acquired on the MERLIN Compact, while the microstructure and composition of the devices were studied by transmission electron microscopy (TEM) and energy-dispersive x-ray spectroscopy (EDS).

Supporting Information

Supporting Information is available from the Wiley Online Library or from the author.

Acknowledgements

This work was supported by the National Key R&D Program of China (2017YFA0207600), National Natural Science Foundation of China (61925401, 92064004, and 61927901), Project 2019BD002 and 2020BD010 supported by PKU-Baidu Fund, and the 111 Project (B18001). Y.Y. acknowledges the support from the Fok Ying-Tong Education Foundation, Beijing Academy of Artificial Intelligence (BAAI), and the Tencent Foundation through the XPLORER PRIZE.

Conflict of Interest

The authors declare no conflict of interest.

Data Availability Statement

The data that support the findings of this study are available from the corresponding author upon reasonable request.

Keywords

artificial astrocyte, image recognition, memristor, neuromorphic computing, nonlinearity

Received: July 2, 2021
Revised: August 14, 2021
Published online:

[1] M. Horowitz, *IEEE Int. Solid-State Circuits Conf. Dig. Tech. Pap.* **2014**, *57*, 10.
[2] J. Backus, *Commun. ACM* **1978**, *21*, 613.
[3] M. M. Waldrop, *Nature* **2016**, *530*, 144.
[4] C. Mead, *Proc. IEEE* **1990**, *78*, 1629.
[5] T. K. Zhou, X. Lin, J. Wu, Y. Chen, H. Xie, Y. Li, J. Fan, H. Wu, L. Fang, Q. Dai, *Nat. Photonics* **2021**, *15*, 367.
[6] K. Roy, A. Jaiswal, P. Panda, *Nature* **2019**, *575*, 607.
[7] D. Strukov, G. Indiveri, J. Grollier, S. Fusi, *Nat. Commun.* **2019**, *10*, 4838.
[8] I. Boybat, M. L. Gallo, S. R. Nandakumar, T. Moraitis, T. Parnell, T. Tuma, B. Rajendran, Y. Leblebici, A. Sebastian, E. Eleftheriou, *Nat. Commun.* **2018**, *9*, 2514.

[9] M. M. Waldrop, *Nature* **2013**, *503*, 22.
[10] G. W. Burr, R. M. Shelby, A. Sebastian, S. Kim, S. Kim, S. Sidler, K. Virwani, M. Ishii, P. Narayanan, A. Fumarola, L. L. Sanches, L. Boybat, M. L. Gallo, K. Kibong Moon, J. Woo, H. Hwang, Y. Leblebici, *Adv. Phys.: X* **2017**, *2*, 89.
[11] D. Ielmini, H. S. P. Wong, *Nat. Electron.* **2018**, *1*, 333.
[12] N. K. Upadhyay, H. Jiang, Z. Wang, S. Asapu, Q. Xia, J. J. Yang, *Adv. Mater. Technol.* **2019**, *4*, 1800589.
[13] V. K. Sangwan, M. C. Hersam, *Nat. Nanotechnol.* **2020**, *15*, 517.
[14] A. Sebastian, M. L. Gallo, R. Khaddam-Aljameh, E. Eleftheriou, *Nat. Nanotechnol.* **2020**, *15*, 529.
[15] J. Zhu, T. Zhang, Y. Yang, R. Huang, *Appl. Phys. Rev.* **2020**, *7*, 011312.
[16] M. A. Zidan, J. P. Strachan, W. D. Lu, *Nat. Electron.* **2018**, *1*, 22.
[17] Y. Zhang, Z. Wang, J. Zhu, Y. Yang, M. Rao, W. Song, Y. Zhuo, X. Zhang, M. Cui, L. Shen, R. Huang, J. J. Yang, *Appl. Phys. Rev.* **2020**, *7*, 011308.
[18] C. Li, D. Belkin, Y. Li, P. Yan, M. Hu, N. Ge, H. Jiang, E. Montgomery, P. Lin, Z. Wang, W. Song, J. P. Strachan, M. Barnell, Q. Wu, R. S. Williams, J. J. Yang, Q. Xia, *Nat. Commun.* **2018**, *9*, 2385.
[19] T. F. Schranghamer, A. Oberoi, S. Das, *Nat. Commun.* **2020**, *11*, 5474.
[20] L. Liu, W. Xiong, Y. Liu, K. Chen, Z. Xu, Y. Zhou, J. Han, G. Ye, X. Chen, Z. Song, M. Zhu, *Adv. Electron. Mater.* **2020**, *6*, 1901012.
[21] P. M. Sheridan, F. Cai, C. Du, W. Ma, Z. Zhang, W. D. Lu, *Nat. Nanotechnol.* **2017**, *12*, 784.
[22] Q. Duan, Z. Jing, X. Zou, Y. Wang, K. Yang, T. Zhang, S. Wu, R. Huang, Y. Yang, *Nat. Commun.* **2020**, *11*, 3399.
[23] C. Stöckl, W. Maass, *Nat. Mach. Intell.* **2021**, *3*, 230.
[24] G. Q. Bi, M. M. Poo, *J. Neurosci.* **1998**, *18*, 10464.
[25] S. F. Cooke, T. V. Bliss, *Brain* **2006**, *129*, 1659.
[26] A. Araque, V. Parpura, R. P. Sanzgiri, P. G. Haydon, *Trends Neurosci.* **1999**, *22*, 208.
[27] G. Perea, M. Navarrete, A. Araque, *Trends Neurosci.* **2019**, *32*, 421.
[28] M. Arizono, V. K. Inavalli, A. Panatier, T. Pfeiffer, J. Angibaud, F. Levet, M. J. T. Ter Veer, J. Stobart, L. Bellocchio, K. Mikoshiba, G. Marsicano, B. Weber, S. H. R. OlietN, U. V. ägerl, *Nat. Commun.* **2020**, *11*, 1906.
[29] A. Pimenov, J. Ullrich, P. Lunkenheimer, A. Loidl, C. H. Rüscher, *Solid State Ionics* **1998**, *109*, 111.
[30] N. K. Upadhyay, W. Sun, P. Lin, S. Joshi, R. Midya, X. Zhang, Z. Wang, H. Jiang, J. H. Yoon, M. Rao, M. Chi, Q. Xia, J. J. Yang, *Adv. Electron. Mater.* **2020**, *6*, 1901411.
[31] C. Cheng, Y. Li, T. Zhang, Y. Fang, J. Zhu, K. Liu, L. Xu, Y. Cai, X. Yan, Y. Yang, R. Huang, *J. Appl. Phys.* **2018**, *124*, 152103.
[32] A. V. Emelyanov, K. E. Nikiruy, V. A. Demin, V. V. Rylkov, A. I. Belov, D. S. Korolev, E. G. Gryaznov, D. A. Pavlov, O. N. Gorshkov, A. N. Mikhaylov, P. Dimitrakis, *Microelectron. Eng.* **2019**, *215*, 110988.
[33] A. V. Yakimov, D. O. Filatov, O. N. Gorshkov, D. A. Antonov, D. A. Liskin, I. N. Antonov, A. V. Belyakov, A. V. Klyuev, A. Carollo, B. Spagnolo, *Appl. Phys. Lett.* **2019**, *114*, 253506.
[34] T. S. Lee, N. J. Lee, H. Abbas, H. H. Lee, T. S. Yoon, C. J. Kang, *ACS Appl. Electron. Mater.* **2020**, *2*, 1154.
[35] M. J. Lee, C. B. Lee, D. Lee, S. R. Lee, M. Chang, J. H. Hur, Y. B. Kim, C. J. Kim, D. H. Seo, S. Seo, U.-I. Chung, I.-K. Yoo, K. Kim, *Nat. Mater.* **2011**, *10*, 625.
[36] S. Lee, D. Lee, J. Woo, E. Cha, J. Park, H. Hwang, *IEEE Electron Device Lett.* **2014**, *35*, 1022.
[37] J. J. Yang, M. X. Zhang, M. D. Pickett, F. Miao, J. Paul Strachan, W. Li, W. Yi, D. A. A. Ohlberg, B. Joon Choi, W. Wu, J. H. Nickel, G. Modeiros-Ribeiro, R. S. Williams, *Appl. Phys. Lett.* **2012**, *100*, 113501.
[38] W. Zhang, X. Peng, H. Wu, B. Gao, H. He, Y. Zhang, S. Yu, H. Qian, *56th ACM/IEEE Design Automation Conf*, IEEE, Las Vegas, USA **2019**, p. 1.
[39] Y. Yang, X. Zhang, L. Qin, Q. Zeng, X. Qiu, R. Huang, *Nat. Commun.* **2017**, *8*, 15173.
[40] A. Wedig, M. Luebben, D.-Y. Cho, M. Moors, K. Skaja, V. Rana, T. Hasegawa, K. K. Adepalli, B. Yildiz, R. Waser, I. Valov, *Nat. Nanotechnol.* **2016**, *11*, 67.
[41] Z. Wei, Y. Kanzawa, K. Arita, Y. Katoh, K. Kawai, S. Muraoka, S. Mitani, S. Fujii, K. Katayama, M. Lijima, T. Mikawa, T. Ninimiya, R. Miyanaga, Y. Kawashima, K. Tsuji, A. Himemo, T. Okada, R. Azuma, K. Shimakawa, H. Sugaya, T. Takagi, R. Yasuhara, K. Horiba, H. Kumigashira, M. Oshima, *Int. Electron Devices Meet*, IEEE, San Francisco, USA **2008**, p. 293.
[42] J. Chen, C. Huang, C. Chiu, Y. Huang, W. Wu, *Adv. Mater.* **2015**, *27*, 5028.
[43] H. Manem, G. S. Rose, X. He, W. Wang, *Proc. of the 20th Symposium on Great Lakes Symposium on VLSI*, IEEE, Rhode Island, USA **2010**, p. 287.
[44] Y. Yang, P. Gao, S. Gaba, T. Chang, X. Pan, W. Lu, *Nat. Commun.* **2012**, *3*, 732.
[45] K. Krishnan, T. Tsuruoka, C. Mannequin, M. Aono, *Adv. Mater.* **2016**, *28*, 640.
[46] X. Li, J. Tang, Q. Z., B. Gao, J. J. Yang, S. Song, W. Wu, W. Zhang, P. Yao, N. Deng, L. D., Y. Xie, H. Qian, H. Wu, *Nat. Nanotechnol.* **2020**, *15*, 776.
[47] T. Kim, H. Kim, J. Kim, J.-J. Kim, *IEEE Electron Device Lett.* **2017**, *38*, 1228.

